Journal of Energy Storage 101 (2024) 113819

Contents lists available at ScienceDirect

Journal of Energy Storage

journal homepage: www.elsevier.com/locate/est

Research papers

A facile physics-based model for non-destructive diagnosis of battery degradation

Zhenya Wang [a,b], Dmitri L. Danilov [a,c,*], Zhiqiang Chen [a,c,e], Rüdiger-A. Eichel [a,b], Peter H.L. Notten [a,c,d,**]

[a] Forschungszentrum Jülich (IET-1), D-52425 Jülich, Germany
[b] Institute of Physical Chemistry, RWTH Aachen University, D-52074 Aachen, Germany
[c] Eindhoven University of Technology, P.O. Box 513, Eindhoven, 5600 MB, the Netherlands
[d] University of Technology Sydney, Broadway, Sydney, NSW 2007, Australia
[e] CATL Future Energy Research Institute, Shanghai 200235, China

ARTICLE INFO

Keywords:
Lithium-ion batteries
Degradation
Modeling aging
Diagnostic

ABSTRACT

The identification of battery degradation is of significant importance for estimating the state of health. Loss of lithium inventory (LLI), loss of active materials of the negative electrodes (LAMNE), and loss of active materials of the positive electrodes (LAMPE) are three main degradation modes. This paper proposes an advanced model based on open circuit voltage and differential voltage (DV) fitting to diagnose and quantify the degradation modes of batteries at different stages, showing high fidelity. This physics-based model avoids solving many partial differential equations and is not computationally demanding. Using commercial batteries with NCA/SiC electrodes as a case study, the LLI, LAMPE, and LAMNE induced by battery cycling and storage at various temperatures, State-of-Charge, and charging/discharging rates are systematically identified and analyzed.

1. Introduction

Lithium-ion batteries (LIBs) have played an essential role in power storage systems, consumer electronics, the transportation industry, etc. Presently, the growing demand for electric vehicles and electrochemical energy storage systems continues to accelerate the large-scale applications of LIBs [1–3]. Nevertheless, the degradation of LIBs limits the lifespan and power performance and even causes safety hazards [4–7]. The prerequisite for addressing these issues is an ability to precisely diagnose these batteries' state of health (SoH) and degradation modes.

The degradation of LIBs can be attributed to various chemical and physical modes that affect the various components of LIBs [8–10]. The main degradation modes of lithium-ion batteries can be classified as follows: loss of lithium inventory (LLI), loss of active materials of the negative electrodes (LAMNE), and loss of active materials of the positive electrodes (LAMPE) [11–20]. Specifically, lithium ions are consumed by side reactions, such as SEI growth, lithium plating, etc. These ions are, therefore, no longer available for cycling between the positive and negative electrodes. That is denoted as an LLI and leads to capacity losses. Lithium-ion immobilization in electronically isolated particles of the active electrode materials can also contribute to LLI.

LAMNE means that the active material in the negative electrode becomes unavailable for lithium insertion due to particle cracking, binder decomposition, or the obstruction of active sites by resistive surface layers. That degradation mechanism can result in both capacity and power fading, as they hinder lithium ions intercalation and deintercalation.

LAMPE means that the active material in the positive electrode becomes unavailable due to structural disordering, particle cracking, transition metal dissolution, or loss of electrical contact. In addition, a rise in electrode resistance or loss of electrode conductivity can also affect the kinetic performance of Li-ion batteries because they affect the electron transport rate through the electrodes, which in turn affects the charging and discharging rate and overall performance of the batteries [21–23].

Typically, experimentally analyzing battery degradation implies the destructive disassembly of batteries and requires specialized laboratory equipment, incurring long time and high financial costs. Consequently,

---

* Corresponding author at: Forschungszentrum Jülich (IET-1), D-52425 Jülich, Germany.
** Corresponding author at: Eindhoven University of Technology, P.O. Box 513, Eindhoven 5600 MB, the Netherlands.
E-mail addresses: d.danilov@fz-juelich.de (D.L. Danilov), p.h.l.notten@tue.nl (P.H.L. Notten).

https://doi.org/10.1016/j.est.2024.113819
Received 5 June 2024; Received in revised form 10 August 2024; Accepted 13 September 2024

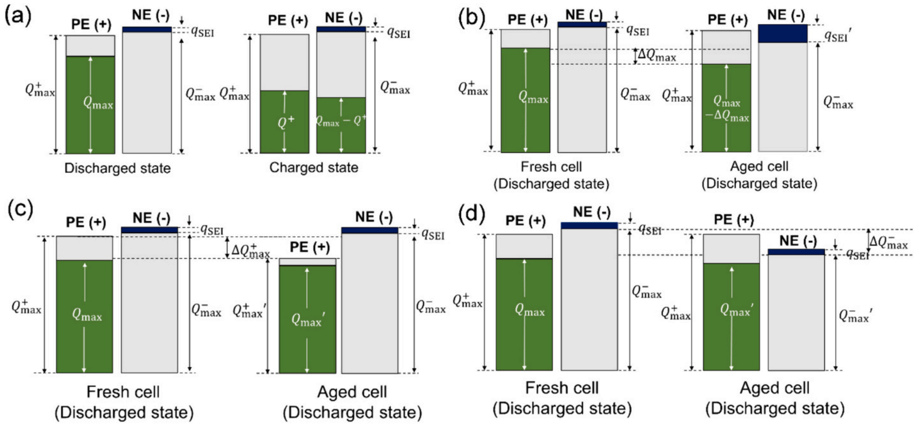

Fig. 1. Schematic representation of (a) a pristine cell, (b) an LLI-induced degraded cell, (c) an LAMPE-induced degraded cell, and (d) an LAMNE-induced degraded cell.

the experimental analysis is almost impossible to implement in battery management systems of electric vehicles [5,13,16,17,24,25]. On the other hand, non-destructive diagnostic approaches based on in-situ measurements are widely acknowledged as a powerful and convenient tool for extracting battery degradation characteristics. Those include voltage fitting, incremental capacity (IC) analysis, electrochemical impedance spectroscopy (EIS) analysis, and differential voltage (DV) analysis.

The open circuit voltage (OCV) is the difference between the anode and cathode voltages under non-loading equilibrium conditions, which provides thermodynamic battery properties. The changes in OCV can be used to evaluate the State-of-Charge (SoC), SoH, or degradation characteristics [13–15,26–29]. Since the real OCV is not easy to measure, the voltage profile obtained when the current is very small (less than 0.04C) is frequently considered equivalent to the OCV profile. Such voltage is called pseudo-OCV [10,14]. Under OCV (or pseudo-OCV) test conditions, conductivity losses due to ohmic resistance or overpotential are usually ignored. Numerous contemporary methods for OCV fitting rely on either equivalent circuit models or data-driven models. The former method proves challenging in comprehensively elucidating the intricate electrochemical processes within batteries, whereas the latter method demands a substantial volume of training data and computational resources [13,30–34]. EIS tests have a relatively short duration and can provide detailed information about the internal state of the battery when measurements are made at specific frequencies and SoCs. But the data analysis requires sophisticated equipment and expertise, including fitting the models, and has high signal processing requirements. Different batteries may require different models. IC or DV analysis, as an alternative approach, converts voltage plateaus into apparent peaks to extract the degradation of LIBs [31,32,35–37]. However, at high or low (dis)charge rates, more pronounced polarization effects or noise are prone to be generated, which needs data filtering and smoothing, further deforming IC and DV curves and affecting the accuracy of these methods [10,38,39]. Overall, these diagnostic methods have been successfully used to analyze the degradation of LIBs. Still, the relation between the degradation modes at various temperatures, (dis)charging rates, and SoCs has not yet been systematically explained.

In this paper, a novel physics-based approach is proposed for OCV fitting and unraveling the degradation modes, which avoids the complex partial differential equations of traditional electrochemical models and does not rely on large amounts of training data, thereby saving computational resources. Moreover, this model also simultaneously incorporates the fitting of DV curves to improve accuracy and show high fidelity. Subsequently, LLI, LAMPE, and LAMNE are extracted to systematically analyze calendar and cycling-induced aging under various temperatures, SoCs, and (dis)charging rates, respectively. The research is carried out using the latest generation of high-energy-density NCA/Si-C cylindrical batteries.

2. Experimental

2.1. Storage measurements of cylindrical batteries

Calendar storage measurements utilized commercial 18650-type cylindrical batteries fabricated by Tianjin Lishen Battery Co., Ltd. with a nominal capacity of 3.2 Ah. Before the storage, all batteries underwent cycling with a 0.3C (1C = 3.2 A) current for 50 cycles within the voltage range of 2.7–4.2 V to establish a stable Solid Electrolyte Interphase (SEI). That was followed by cycles with 0.01C to acquire the pseudo-open-circuit voltage (OCV) curves. The batteries were subsequently stored at 20 %, 50 %, and 100 % of the SoC at 25 °C. OCV assessments were conducted every 30 days during the storage period. After that, the batteries were recharged to the corresponding SoC to prolong the storage tests. At 10 °C and 45 °C, the batteries were stored at 50 % SoC.

2.2. Cycling measurements of cylindrical batteries

Before the experiments, all 18650-type batteries underwent activation through four cycles employing constant-current constant-voltage (CCCV) charging and constant-current (CC) discharging within a voltage range of 2.7–4.2 V. A current of 0.3C was applied in CC mode, with a cut-off current for CV mode set at 0.04C. Subsequently, cycles with 0.01C were conducted to obtain pseudo-OCV curves for the batteries. After that, cycling tests were executed with a consistent charging current of 0.3C or 1C, while the discharging C-rates of 0.1, 0.5, 1, and 2C were used. Throughout the cycling process, all batteries underwent charging in CCCV mode. Discharging was performed in CC mode until reaching 2.7 V. A 30-minute relaxation period was made between the charging and discharging steps. Cycles to determine OCV curves were systematically conducted at 50 or 100 cycles during the cycling. The temperatures for the cycling measurements were maintained at 10, 25, and 45 °C.

2.3. Coin-type cell measurements

Cylindrical batteries were disassembled within an argon-filled glove box, and some parts of the anodes and cathodes were cut out. One side of the anodes and cathodes underwent meticulous scraping with a sharp blade. Foils were cut into discs of 14 mm in diameter. The anode and cathode discs were individually assembled into coin cells, employing metallic Li as counter electrodes. Celgard 2400 served as a separator, while the electrolyte comprised 1 M $LiPF_6$ dissolved in a solvent mixture of EC:DMC:DEC (1:1:1, volume ratio). The electrochemical characteristics of the coin cells were investigated utilizing a Neware battery test system, spanning the voltage range of 0.01–2 V for the anode and 2.8–4.3 V for the cathode versus Li at 25 °C. Before each experiment, a 12-hour equilibration period was ensured, followed by four activation cycles with a 0.2C-rate current (1C = 7 mA). Subsequently, the pseudo-open-circuit voltage (OCV) was determined at 0.01C-rate.

3. Model development

Fig. 1 shows the layout of pristine and degraded cells, revealing the changes in LLI, LAMPE, and LAMNE. The following three parameters determine the degree of aging of a particular cell at any moment: the maximum capacity of the negative electrode $Q^{-}_{\max}$, the maximum capacity of the positive electrode $Q^{+}_{\max}$, and the amount of electrochemically active lithium $Q_{\max}$. For a cell just after production but before activation $Q_{\max} = Q^{+}_{\max}$ because all lithium was introduced to the Li-ion cell by the cathode. After activation and subsequent discharge, $Q_{\max}$ reduces due to lithium consumption in the solid electrolyte interphase (SEI). The amount of charge of lithium-ions consumed in this process is denoted q_{SEI}, as illustrated in Fig. 1. Define

$$x_{SEI} = \frac{q_{SEI}}{Q^{+}_{\max}}, \tag{1}$$

in which x_{SEI} gives the fraction of initially available Li captured in SEI. Then, the total amount of electrochemically active lithium after full activation is $(1 - x_{SEI})Q^{+}_{\max}$. Please note that a small amount of lithium ions may remain in the negative electrode (NE) in the completely discharged state due to various kinetic limitations. Usually, it is small (1–2 %) and, therefore, omitted in Fig. 1b-d.

Define Q^{-} and Q^{+} as the amounts of lithium stored inside the negative and positive electrodes accordingly, at any arbitrary state, then

$$y = \frac{Q^{-}}{Q^{-}_{\max}}, \tag{2}$$

$$x = \frac{Q^{+}}{Q^{+}_{\max}}, \tag{3}$$

where y and x are the normalized lithium content in the corresponding electrode. Those are functions of SoC. From the mass conservation law, it follows that at any moment in time

$$Q^{-} + Q^{+} = Q_{\max}. \tag{4}$$

Therefore, the voltage of the battery must obey a system of equations

$$\begin{cases} E_{bat}(Q^{+}, Q^{-}) = E_p\left(\dfrac{Q^{+}}{Q^{+}_{\max}}\right) - E_n\left(\dfrac{Q^{-}}{Q^{-}_{\max}}\right) \\ Q^{-} + Q^{+} = Q_{\max} \end{cases}, \tag{5}$$

where E_p and E_n are voltages of positive and negative electrodes as a function of x and y, respectively, and E_{bat} is the battery voltage. Express Q^{-} as a function of Q^{+} according to

$$Q^{-} = Q_{\max} - Q^{+}. \tag{6}$$

Then substitute Eq. (6) into the first equation of the system Eq. (5) to obtain the (equilibrium) voltage of the battery as a function of a single variable Q^{+}:

$$E_{bat}(Q^{+}) = E_p\left(\frac{Q^{+}}{Q^{+}_{\max}}\right) - E_n\left(\frac{Q_{\max} - Q^{+}}{Q^{-}_{\max}}\right). \tag{7}$$

Two other parameters are cut-off voltages E^{up} and E^{down}. They correspond to the voltages at which the battery is considered completely charged and completely discharged accordingly. Define Q^{+}_{down} and Q^{+}_{up} as solutions of the system of equations:

$$\begin{cases} E^{up} = E_p\left(\dfrac{Q^{+}_{up}}{Q^{+}_{\max}}\right) - E_n\left(\dfrac{Q_{\max} - Q^{+}_{up}}{Q^{+}_{\max}}\right) \\ E^{down} = E_p\left(\dfrac{Q^{+}_{down}}{Q^{+}_{\max}}\right) - E_n\left(\dfrac{Q_{\max} - Q^{+}_{down}}{Q^{+}_{\max}}\right) \end{cases}. \tag{8}$$

Q^{+}_{down} corresponds to the absolute lithium content in the positive electrode when the battery is considered to be (completely) discharged while Q^{+}_{up} corresponds to the completely charged state. Then, the operational capacity of the battery Q_{cap} is a difference between Q^{+}_{up} and Q^{+}_{down}, i.e.

$$Q_{cap} = Q^{+}_{down} - Q^{+}_{up}. \tag{9}$$

The capacity of the battery, as given by Eq. (10) is a function of $Q^{+}_{\max}$, $Q^{-}_{\max}$ and $Q_{\max}$, but, strictly speaking, also depends on $x_{\min}$, x_{SEI}, E^{up} and E^{down}, i.e.

$$Q_{cap} = Q_{cap}\left(Q^{+}_{\max}, Q^{-}_{\max}, Q_{\max}; x_{\min}, x_{SEI}, E^{up}, E^{down}\right). \tag{10}$$

This analytical model is highly flexible and can explain a variety of scenarios. However, due to the design of our aging experiments, the last four parameters can usually be regarded as constants. Thus,

$$E_{bat}(Q^{+}) = E_p\left(\frac{Q^{+}}{Q^{+}_{\max}}\right) - E_n\left(\frac{Q_{\max} - Q^{+}}{Q^{-}_{\max}}\right), \qquad Q^{+}_{up} \le Q^{+} \le Q^{+}_{down}. \tag{11}$$

The layered Li[Ni$_a$Co$_b$Al$_{1\text{-}a\text{-}b}$]O$_2$ (NCA) is one of the most promising materials used for positive electrodes due to its high energy density, good stability, and low cost [40–42]. By increasing the Ni content and reducing the Co content, the demand for higher energy density and lower cost of transition metal layered oxide cathode materials can be met. However, the increase in Ni content is accompanied by decreased structural and thermal stability due to weaker Ni—O bonds, leading to poorer cycling performance and accelerated material failure at high voltages [43–45]. For the negative electrode, graphite-based composite materials such as graphite-Si or graphite-SiO$_z$ are widely used to improve energy densities [46]. In this paper, the positive and negative materials of the studied batteries are Li[NCA]O$_2$ and blended SiC, respectively. It is worth noting that there should be a minimum number x_{min} of x since lithium ions in the layered cathode materials can not be extracted fully to maintain structural stability and avoid safety hazards. For instance, x_{min} can be around 0.55 for LiCoO$_2$ [47,48] and about 0.3 for NCA [49].

The equilibrium voltages measured with respect to a Li reference electrode as a function of extracted charge, i.e. a set of pairs (q_i^{+},E_i^{+}) and (q_i^{-},E_i^{-}), is shown in Fig. S1 from the supporting file. The red line represents the NCA electrode, and the blue line is the composite SiC electrode. The lithium content is recovered from the extracted charge according to

$$y_i = \frac{\max\limits_i(q_i^{-}) - q_i^{-}}{\max\limits_i(q_i^{-})} \tag{12}$$

for the negative electrode and

$$x_i = \frac{x_{\min}\frac{\max_i(q_i^{+})}{1 - x_{\min} - x_{SEI}} + q_i^{+}}{\frac{\max_i(q_i^{+})}{1 - x_{\min} - x_{SEI}}} \tag{13}$$

for the positive electrode. By direct substitution, it is easy to see that for the negative electrode $q_i^{-} = 0$ implies $y_i = 1$ (fully lithiated material) and $q_i^{-} = \max\limits_i(q_i^{-})$ implies $y_i = 0$. For the positive electrode $q_i^{+} = 0$ implies that $x_i = x_{\min}$ and $q_i^{+} = \max\limits_i(q_i^{+})$, implying that $x_i = 1 - x_{SEI}$. That corresponds to the situation when both electrodes can be fully charged and discharged, but the lithium ions immobilized in SEI are removed from (dis)charging cycles. Thus, the experimental data is

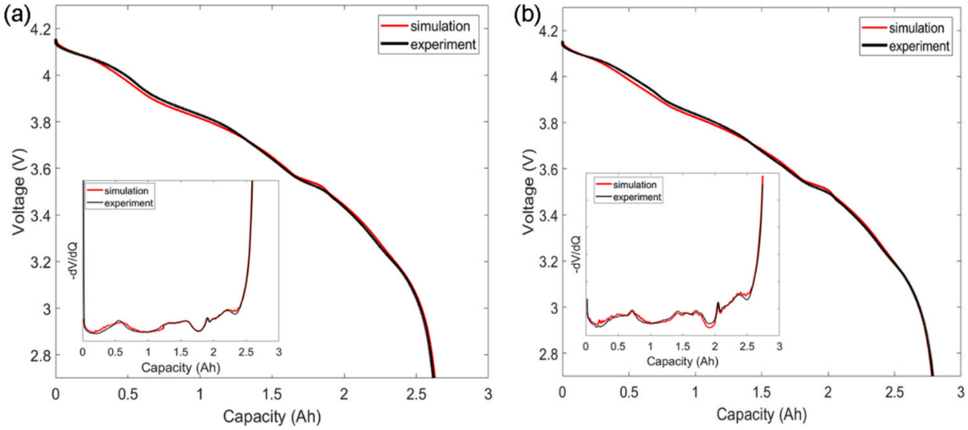

Fig. 2. Simulated (red curves) and experimental (black curves) results of the (pseudo) OCV curve (a) for a battery at 50 % SoC that underwent calendar aging of 200 days at 45 °C, and (b) for a battery after 200 cycles (dis)charged at 0.5C, 25 °C. Insets are the simulated and experimental results for the differential voltage curves. (For interpretation of the references to colour in this figure legend, the reader is referred to the web version of this article.)

transformed into sets of pairs (x_i,E_i^+) and (y_i,E_i^-). Define two functions to perform interpolation on the base of (x_i,E_i^+) and (y_i,E_i^-), namely $E_p(x)$ and $E_n(y)$. Outside of the sampling interval, linear extrapolation is adopted, which simplifies programming and gives more stable calculations.

Finally, the operational capacity and voltage are related to $Q_{\max}^+$, $Q_{\max}^-$, and $Q_{\max}$, which correspond to LAMPE, LAMNE, and LLI, respectively. The fitting procedure was executed in MATLAB utilizing the *fminsearch* optimization function. In addition, the corresponding differential voltage curves were simultaneously taken into consideration to improve the accuracy of this model further. The root-mean-square error (RMSE) of OCV and DV, shown in Eqs. (14) and (15), are calculated firstly, according to

$$RMSE_{OCV} = \sqrt{\frac{1}{n}\sum_{i=1}^{n}\left(OCV'_i - OCV_i\right)^2}, \tag{14}$$

$$RMSE_{DV} = \sqrt{\frac{1}{n}\sum_{i=1}^{n}\left(DV'_i - DV_i\right)^2}, \tag{15}$$

where OCV'_i denotes the modeled values of the OCV curve, OCV_i represents the experimental values and n is the number of measured values. The same holds for DV'_i and DV_i. The summation of these terms is used for the optimization process, i.e.

$$RMSE = \omega RMSE_{OCV} + (1-\omega)RMSE_{DV}, \tag{16}$$

where ω represents the weight factor adjusting the fitting results in favour of the OCV or DV. Moreover, a multi-start optimization approach was implemented to enhance the capacity for identifying the global minimum. A Monte Carlo algorithm was employed for the generation of diverse starting values, and the Nelder-Mead algorithm was subsequently applied to each initial value, from which the optimal solution was selected.

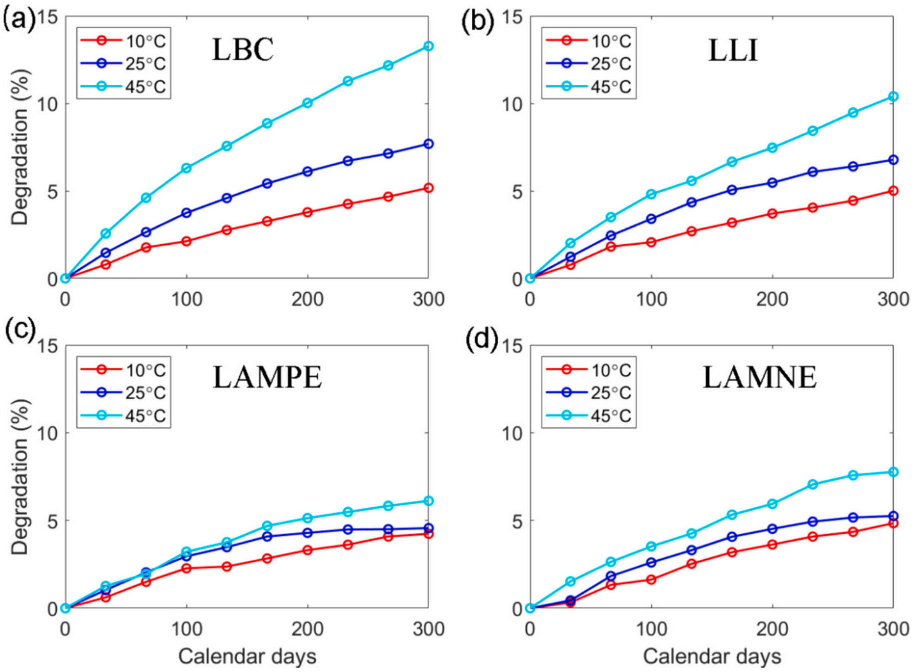

Fig. 3. Degradation of (a) total battery capacity, (b) LLI, (c) LAMPE, and (d) LAMNE for the batteries at 50 % SoC during calendar aging at different indicated temperatures.

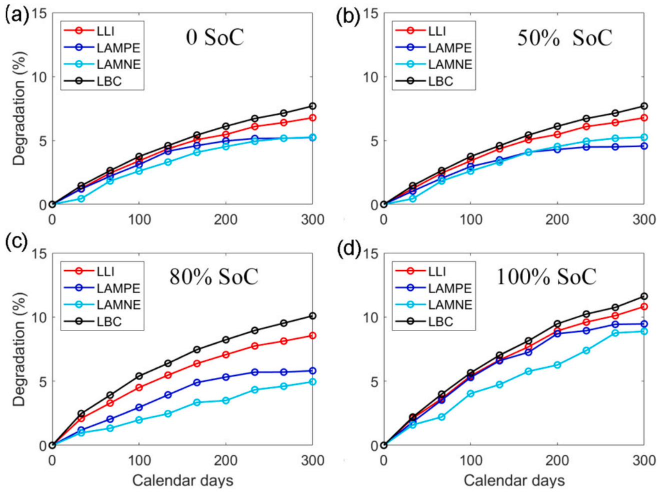

Fig. 4. Battery degradation at (a) 0, (b) 50, (c) 80, and (d) 100 % SoC at 25 °C.

4. Results and discussion

The OCV and DV curves for all experimental results are reconstructed based on the proposed model described above. A typical example of the modeled and experimental results is shown in Fig. 2. Fig. 2a illustrates the (pseudo) OCV curves of the battery at 50 % SoC that underwent calendar aging of 200 days at 45 °C. Fig. 2b shows the results of another battery after 200 cycles with a (dis)charge current of 0.5C at 25 °C. The inset images are the corresponding DV curves. The red lines represent the simulations, and the black lines are the experimental results. It can be observed that both the OCV and DV curves are fitted very well, regardless of calendar aging or cycling-induced aging. Specifically, the errors between the modeled and experimental OCV of both plots are no more than 0.2 %. The precise fit for OCV and DV ensures the accuracy of the extracted battery degradation modes.

4.1. Storage-induced degradation

The degradation modes of commercial 18650 batteries at the same SoC during calendar aging at different temperatures are analyzed using the proposed diagnostic method. All degradation (capacity loss) percentages are normalized with respect to the pristine battery capacity and are shown in Fig. 3. Fig. 3a shows the battery capacity loss (LBC) during calendar aging. It is evident that the higher the temperature during storage, the faster the battery degradation occurs. Battery capacity degradation after 300 days of storage was 4.8, 6.5, and 13.3 % at 10, 25, and 45 °C, respectively. That is because the high temperature accelerates many side reactions, such as the SEI growth and the electrolyte decomposition, and promotes the dissolution of electrode materials [50–52]. As shown in Fig. 3a, the capacity decay rate stabilizes in the later stages at storage temperatures of 10 and 25 °C. However, this trend was not observed at 45 °C, where the battery degrades at a higher rate. LLI, LAMNE, and LAMPE are shown in Fig. 3b-d, respectively. In general, all three degraded the most at 45 °C. As shown in Fig. 3, degradation due to LLI is larger than that of LAMNE and LAMPE because the electrode material structure does not change much without cycling. The trend of LLI is also the closest to LBC, indicating that LLI is the main factor of battery degradation. The consumption of recyclable lithium ions can be attributed mainly to the continuous SEI growth [24,53,54]. High temperatures accelerate this electrochemical process because of the higher rate of electron tunneling induced by a lower energy barrier [50].

The degradation of batteries stored at different SoCs at 25 °C is plotted in Fig. 4. The capacity of all batteries declines over time, but the rate of capacity decline slows down. Previous publications also show this nonlinear relation [55–57]. From Fig. 4, it can be seen that the storage-induced capacity loss is sensitive to the SoC. After 300 days of storage, the battery capacity loss is around 7.1, 7.5, 10.2, and 11.8 %, for 0, 50, 80, and 100 % SoC, respectively. Operation at higher SoC accelerates degradation, which is attributable to the correlation between the electrode potentials and the rate of parasitic side reactions [58,59]. Fig. 4 also suggests that higher SoC leads to a faster decline of LLI and LAM. That has been attributed to particle fracture, lithium plating, structural change [26,52,60,61], etc. More specifically, the NCA is prone to

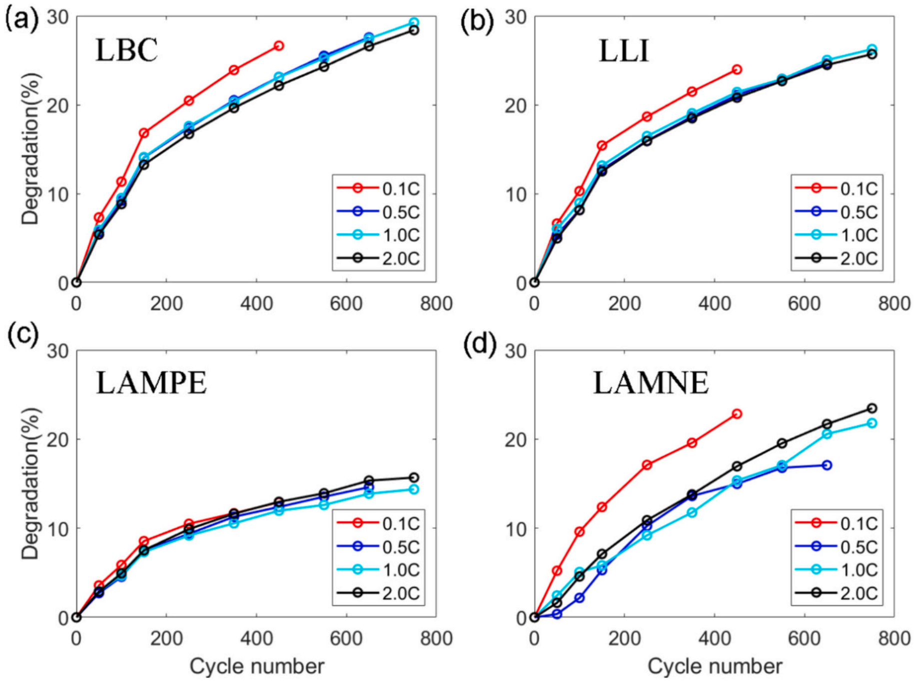

Fig. 5. Battery degradation upon cycling at various discharging currents at 25 °C for (a) LBC, (b) LLI, (c) LAMPE, and (d) LAMNE as a function of cycle number. The batteries are all charged at a current of 0.3 C.

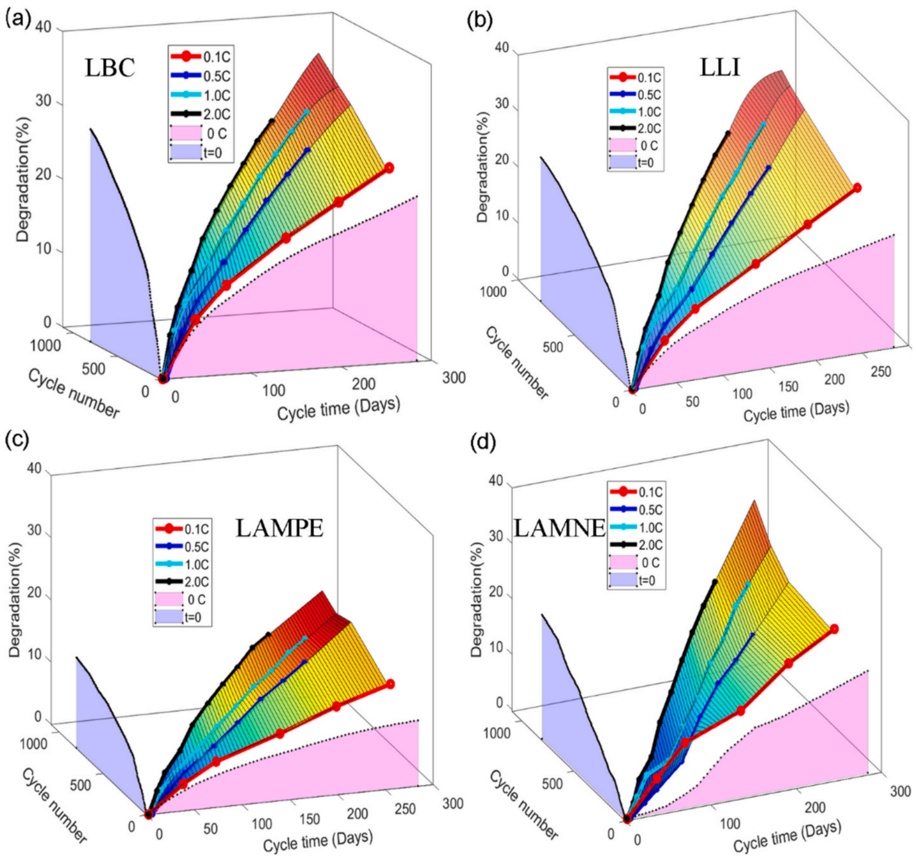

Fig. 6. 3D plots with extrapolation to zero current and zero time for the (a) LBC, (b) LLI, (c) LAMPE, and (d) LAMNE at various discharging currents at 25 °C as a function of cycle number and cycling time. The batteries are all charged at a current of 0.3C.

decomposition since the high degrees of delithiation cause thermodynamic instability and loss of the lattice oxygen.

On the other hand, particle fracturing and/or volume expansion of SiC induced at high SoC results in accelerated LAMNE [11,59,62,63]. That is because the volume change is more significant at high SoCs since more lithium ions are intercalated in the silicon lattice. Consequently, this drastic volume change leads to larger mechanical stresses, resulting in particles cracking. In addition, at high SoCs, the SEI layer is more prone to exfoliation and continuous growth, resulting in isolating the silicon particles from participating in electrochemical reactions, thus further contributing to LAMNE. However, LAMPE and LAMNE have a much larger impact on battery power than on battery capacity, and LLI is usually considered the main contribution to the LBC [64–67]. It can be noticed in Fig. 4 that LLI is the most dominant factor of degradation. The more severe lithium plating induced at high SoC and the continued SEI growth immobilize and consume large amounts of recyclable lithium, resulting in the loss of lithium inventory and, consequently, battery degradation.

4.2. Cycling-induced degradation

Cycling-induced battery degradation is shown in Fig. 5 at different discharging currents. All batteries were charged at 0.3C and then discharged at 0.1, 0.5, 1.0 and 2.0C. It can be seen that degradation at all currents increases with the number of cycles. LAMPE is smaller than LAMNE in this cycling scenario, indicating that the NCA-rate performance is better than that of the SiC electrode. That may be due to the presence of Si, which causes more severe volume expansion and particle crushing. However, there is no significant dependence between the various discharging currents and the number of cycles. As can be seen from Fig. 5, the fastest degradation is observed at a low discharging current of 0.1C, which is most pronounced for LBC and LLI. In contrast, the degradation with the largest discharging current of 2C is moderate. In addition, at the same number of cycles, the effect of different cycling currents on LAMPE and LAMNE is even less noticeable.

Fig. 6 shows a three-dimensional representation of the degradation dependence on the number of cycles and cycling time as a function of cycling current at 25 °C. It can be inferred that, unlike the number of cycles, the cycling current at a given cycle time affects the battery degradation, i.e., the capacity loss shows a clear dependence on the cycling current. The higher the discharging current, the more severe LLI, LAMPE, and LAMNE degradation is as a function of cycling time. That is because batteries at large currents complete more cycles in the same cycling time. In addition, a proficient application of mathematical extrapolation to zero current is executed to discern the temporal impact on cumulative battery degradation while mitigating the influence of cycling effects [68]. For example, the irreversible LBC ascertained through linear extrapolation at low C-rates towards zero current is pure calendar aging, as illustrated in magenta in Fig. 6a. It depends on the cycling time instead of cycling currents or cycle number. Likewise, to mitigate the impact of calendar aging and isolate the exclusive influence of cycling, the cumulative LBC is subjected to mathematical extrapolation to zero time, as delineated by the blue region in Fig. 6a. It increases obviously with the number of cycles and is attributed to the continuous SEI growth. Details of this mathematical extrapolation can be found in the supporting information. The extrapolation clearly reveals that pure cycling-induced battery degradation is much larger than the degradation caused by pure calendar aging. This convenient mathematical extrapolation method allows the effects of cycling time and cycle numbers to be extracted independently from traditional battery cycling experiments, contributing to the analysis of battery aging in greater depth. Figs. 6b-d show that this extrapolation was first applied to

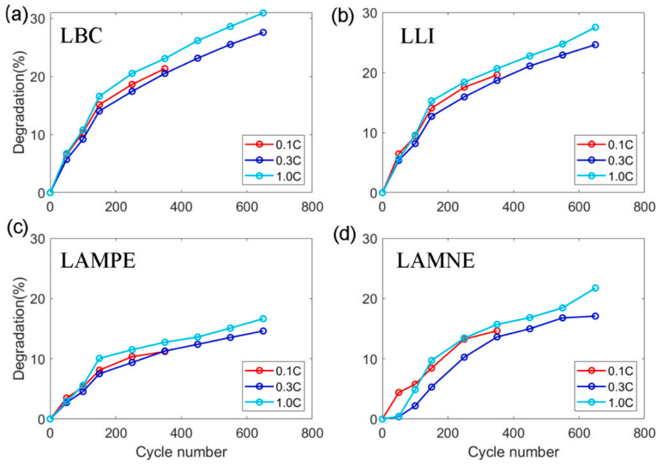

Fig. 7. Battery degradation upon cycling at various charging currents at 25 °C for (a) LBC, (b) LLI, (c) LAMPE, and (d) LAMNE as a function of cycle number. The batteries are all discharged at a current of 0.5 C.

analyze LLI, LAMPE, and LAMNE. It is worth noting that LAMNE grows more slowly in the early stages when extrapolated to zero current. It indicates that the Si/C anode material used in this battery has good stability during the initial period of pure calendar aging.

Moreover, as demonstrated in Fig. 6, the contribution of LLI still plays the dominant role in the capacity loss at 25 °C. Similarly, it is known from the extrapolation region that the LLI due to pure cycling is higher than that due to calendar storage. During the cycling process, volume changes in the anode material cause the SEI to crack, allowing part of the anode surface to be re-exposed to the electrolyte. That induces the continued formation and growth of the SEI layer, consuming a large amount of recyclable lithium [69–71]. High cycling currents and long cycle times facilitate this process. In general, since the battery discharge capacity is equal to the number of cyclable lithium ions moving from the anode to the cathode, LLI is the main factor affecting the discharge capacity of lithium-ion batteries [18,64].

Fig. 7 shows battery degradation at the same discharging current (0.3C) but at various charging rates (0.1, 0.3, and 1.0C) at 25 °C. The curves indicate that high charging rates induce more severe battery degradation than high discharging rates, as shown in Fig. 7. The LBC is more than 30 % after 600 cycles with a charging current of 1C, while it is around 23 % with the same discharging current. LLI and LAMNE are greater than LAMPE at higher charging currents, implying that the cathode material of this Li-ion battery has a better rate performance. High charging currents seem to promote lithium plating and SEI growth [72], thereby consuming lithium inventory.

Additionally, the volume change of the SiC electrode is larger at higher charging rates, leading to particle fracture, isolation, and structural collapse. There are, therefore, not enough sites in the active material to accommodate lithium ions, which results in LAMNE [73]. Furthermore, this process prevents some of the lithium ions inside the active material from being recycled and increases LLI. It can be concluded that the LLI still dominates battery degradation under these conditions.

LBC, LLI, LAMPE, and LAMNE are shown in Fig. 8 at different temperatures during cycling with 0.3C charging and 0.5C discharging. It is clear to see that the capacity loss at 45 °C is about twice that at 10 °C. LLI and LAMPE worsen at increasing temperatures since high temperatures accelerate the SEI growth and decomposition of the positive electrodes [50,52]. It is worth noting that higher temperatures have a more pronounced effect on LAMNE. Degradation resulting from LAMNE plays a more pronounced role when batteries are cycled at high temperatures. The diminished diffusion coefficient typically induces increased diffusion-induced stress due to larger lithium concentration gradients within the particles at low temperatures. That causes particle crack and isolation [74–76]. That could explain why LAMNE is worse at 10 °C than at 25 °C. But at higher temperatures of 45 °C, LAMNE declines more quickly. That can be attributed to accelerated side reactions occurring at the positive electrode, transition metals migrating to the positive electrode, thereby blocking the active lithiation sites [77,78].

5. Conclusions

This paper presents a compact and efficient model for diagnosing battery degradation. LLI, LAMPE, and LAMNE degradation modes for commercial batteries with NCA/SiC electrodes at various temperatures and (dis)charging rates are systematically investigated and quantified by reconstructing the OCV and DV curves. The experimental and modeling results agree very well with each other. Moreover, the degradation due to calendar aging at various temperatures and SoC is also investigated. It

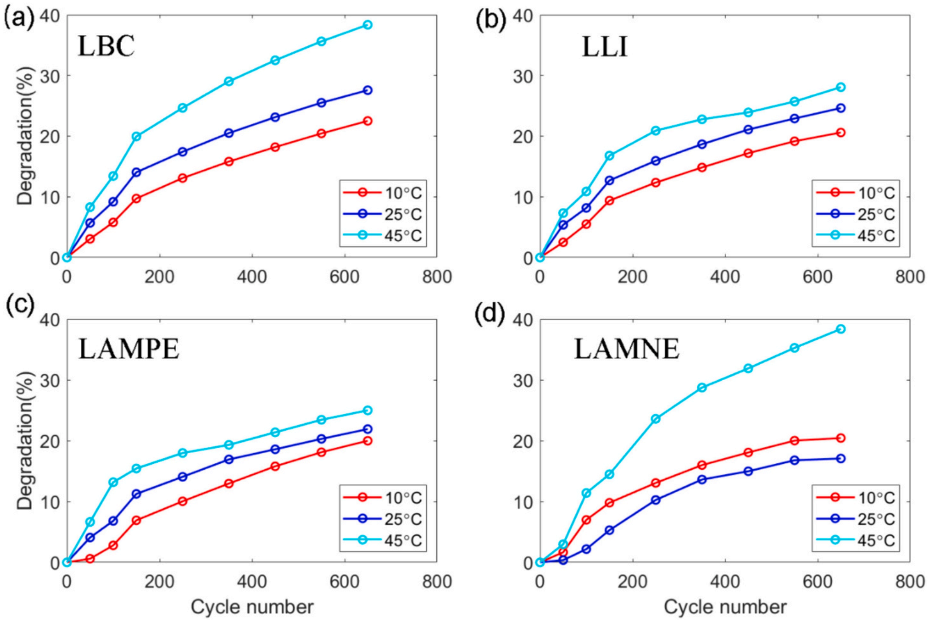

Fig. 8. Battery degradation at various temperatures for (a) LBC, (b) LLI, (c) LAMPE, and (d) LAMNE as a function of cycle number.

can be concluded that battery degradation is accelerated under high temperatures, high SoC, and high (dis)charging rates. LLI is the most dominant degradation mode in most cases, while degradation due to LAMNE is more pronounced when cycling occurs at higher temperatures. The proposed model allows a facile and non-destructive determination of aging modes. That ensures an easy and efficient degradation estimation, which can be adopted for all lithium-ion chemistries.

CRediT authorship contribution statement

Zhenya Wang: Writing – original draft, Validation, Software, Investigation, Data curation. **Dmitri L. Danilov:** Writing – review & editing, Supervision, Software, Methodology, Conceptualization. **Zhiqiang Chen:** Data curation. **Rüdiger-A. Eichel:** Project administration. **Peter H.L. Notten:** Writing – review & editing, Supervision, Conceptualization.

Declaration of competing interest

The authors declare that they have no known competing financial interests or personal relationships that could have appeared to influence the work reported in this paper.

Data availability

Data will be made available on request.

Acknowledgments

Z. Wang gratefully acknowledges the fellowship support by the China Scholarship Council. Dr. D.L. Danilov appreciates the support from the grant ProMoBiS (grant Number. 03ETE046C, BMBF, Germany).

Appendix A. Supplementary data

Supplementary data to this article can be found online at https://doi.org/10.1016/j.est.2024.113819.

References

[1] Z. Cui, A. Manthiram, Thermal stability and outgassing behaviors of high-nickel cathodes in lithium-ion batteries, Angew. Chem. Int. Ed. 62 (2023) e202307243, https://doi.org/10.1002/anie.202307243.

[2] G. Ji, J. Wang, Z. Liang, K. Jia, J. Ma, Z. Zhuang, G. Zhou, H.-M. Cheng, Direct regeneration of degraded lithium-ion battery cathodes with a multifunctional organic lithium salt, Nat. Commun. 14 (2023) 584, https://doi.org/10.1038/s41467-023-36197-6.

[3] T. Montes, F. Pinsach Batet, L. Igualada, J. Eichman, Degradation-conscious charge management: comparison of different techniques to include battery degradation in electric vehicle charging optimization, J. Energy Storage 88 (2024) 111560, https://doi.org/10.1016/j.est.2024.111560.

[4] X.-B. Cheng, R. Zhang, C.-Z. Zhao, Q. Zhang, Toward safe lithium metal anode in rechargeable batteries: a review, Chem. Rev. 117 (2017) 10403–10473, https://doi.org/10.1021/acs.chemrev.7b00115.

[5] H. Wu, H. Jia, C. Wang, J.-G. Zhang, W. Xu, Recent Progress in understanding solid electrolyte interphase on lithium metal anodes, Adv. Energy Mater. 11 (2021) 2003092, https://doi.org/10.1002/aenm.202003092.

[6] Z. Long, L. Yuan, A. Yin, J. Zhou, L. Song, A neural-driven stochastic degradation model for state-of-health estimation of lithium-ion battery, J. Energy Storage 79 (2024) 110248, https://doi.org/10.1016/j.est.2023.110248.

[7] L. Ju, X. Li, G. Geng, Q. Jiang, Degradation diagnosis of lithium-ion batteries considering internal gas evolution, J. Energy Storage 71 (2023) 108084, https://doi.org/10.1016/j.est.2023.108084.

[8] P. Verma, P. Maire, P. Novák, A review of the features and analyses of the solid electrolyte interphase in Li-ion batteries, Electrochim. Acta 55 (2010) 6332–6341, https://doi.org/10.1016/j.electacta.2010.05.072.

[9] S.-K. Jung, H. Gwon, J. Hong, K.-Y. Park, D.-H. Seo, H. Kim, J. Hyun, W. Yang, K. Kang, Understanding the degradation mechanisms of $LiNi_{0.5}Co_{0.2}Mn_{0.3}O_2$ cathode material in lithium ion batteries, Adv. Energy Mater. 4 (2014) 1300787, https://doi.org/10.1002/aenm.201300787.

[10] C.R. Birkl, M.R. Roberts, E. McTurk, P.G. Bruce, D.A. Howey, Degradation diagnostics for lithium ion cells, J. Power Sources 341 (2017) 373–386, https://doi.org/10.1016/j.jpowsour.2016.12.011.

[11] D. Anseán, G. Baure, M. González, I. Cameán, A.B. García, M. Dubarry, Mechanistic investigation of silicon-graphite/$LiNi_{0.8}Mn_{0.1}Co_{0.1}O_2$ commercial cells for non-intrusive diagnosis and prognosis, J. Power Sources 459 (2020) 227882, https://doi.org/10.1016/j.jpowsour.2020.227882.

[12] S. Lee, J.B. Siegel, A.G. Stefanopoulou, J.-W. Lee, T.-K. Lee, Electrode state of health estimation for lithium ion batteries considering half-cell potential change due to aging, J. Electrochem. Soc. 167 (2020) 090531, https://doi.org/10.1149/1945-7111/ab8c83.

[13] X. Bian, L. Liu, J. Yan, Z. Zou, R. Zhao, An open circuit voltage-based model for state-of-health estimation of lithium-ion batteries: model development and validation, J. Power Sources 448 (2020) 227401, https://doi.org/10.1016/j.jpowsour.2019.227401.

[14] J. Tian, R. Xiong, W. Shen, F. Sun, Electrode ageing estimation and open circuit voltage reconstruction for lithium ion batteries, Energy Storage Mater. 37 (2021) 283–295, https://doi.org/10.1016/j.ensm.2021.02.018.

[15] M. Dubarry, C. Truchot, B.Y. Liaw, Synthesize battery degradation modes via a diagnostic and prognostic model, J. Power Sources 219 (2012) 204–216, https://doi.org/10.1016/j.jpowsour.2012.07.016.

[16] B. Stiaszny, J.C. Ziegler, E.E. Krauß, M. Zhang, J.P. Schmidt, E. Ivers-Tiffée, Electrochemical characterization and post-mortem analysis of aged $LiMn_2O_4$–NMC/graphite lithium ion batteries part II: calendar aging, J. Power Sources 258 (2014) 61–75, https://doi.org/10.1016/j.jpowsour.2014.02.019.

[17] B. Stiaszny, J.C. Ziegler, E.E. Krauß, J.P. Schmidt, E. Ivers-Tiffée, Electrochemical characterization and post-mortem analysis of aged $LiMn_2O_4$–$Li(Ni_{0.5}Mn_{0.3}Co_{0.2})O_2$/graphite lithium ion batteries. Part I: cycle aging, J. Power Sources 251 (2014) 439–450, https://doi.org/10.1016/j.jpowsour.2013.11.080.

[18] P.P. Paul, V. Thampy, C. Cao, H.-G. Steinrück, T.R. Tanim, A.R. Dunlop, E.J. Dufek, S.E. Trask, A.N. Jansen, M.F. Toney, J.N. Weker, Quantification of heterogeneous, irreversible lithium plating in extreme fast charging of lithium-ion batteries, Energy Environ. Sci. 14 (2021) 4979–4988, https://doi.org/10.1039/D1EE01216A.

[19] Z. Tong, J. Miao, S. Tong, Y. Lu, Early prediction of remaining useful life for Lithium-ion batteries based on a hybrid machine learning method, J. Clean. Prod. 317 (2021) 128265, https://doi.org/10.1016/j.jclepro.2021.128265.

[20] S. Navidi, A. Thelen, T. Li, C. Hu, Physics-informed machine learning for battery degradation diagnostics: a comparison of state-of-the-art methods, Energy Storage Mater. 68 (2024) 103343, https://doi.org/10.1016/j.ensm.2024.103343.

[21] J. Ma, C. Wang, S. Wroblewski, Kinetic characteristics of mixed conductive electrodes for lithium ion batteries, J. Power Sources 164 (2007) 849–856, https://doi.org/10.1016/j.jpowsour.2006.11.024.

[22] R. Morasch, J. Keilhofer, H.A. Gasteiger, B. Suthar, Methods—understanding porous electrode impedance and the implications for the impedance analysis of Li-ion battery electrodes, J. Electrochem. Soc. 168 (2021) 080519, https://doi.org/10.1149/1945-7111/ac1892.

[23] C. Pastor-Fernández, K. Uddin, G.H. Chouchelamane, W.D. Widanage, J. Marco, A comparison between electrochemical impedance spectroscopy and incremental capacity-differential voltage as Li-ion diagnostic techniques to identify and quantify the effects of degradation modes within battery management systems, J. Power Sources 360 (2017) 301–318, https://doi.org/10.1016/j.jpowsour.2017.03.042.

[24] J.-F. Ding, R. Xu, C. Yan, B.-Q. Li, H. Yuan, J.-Q. Huang, A review on the failure and regulation of solid electrolyte interphase in lithium batteries, J. Energy Chem. 59 (2021) 306–319, https://doi.org/10.1016/j.jechem.2020.11.016.

[25] W.A. Appiah, L.H. Rieger, E. Flores, T. Vegge, A. Bhowmik, Unravelling degradation mechanisms and overpotential sources in aged and non-aged batteries: a non-invasive diagnosis, J. Energy Storage 84 (2024) 111000, https://doi.org/10.1016/j.est.2024.111000.

[26] B. Pan, D. Dong, J. Wang, J. Nie, S. Liu, Y. Cao, Y. Jiang, Aging mechanism diagnosis of lithium ion battery by open circuit voltage analysis, Electrochim. Acta 362 (2020) 137101, https://doi.org/10.1016/j.electacta.2020.137101.

[27] J. Sun, Y. Tang, J. Ye, T. Jiang, S. Chen, S. Qiu, A novel capacity and initial discharge electric quantity estimation method for $LiFePO_4$ battery pack based on OCV curve partial reconstruction, Energy 243 (2022) 122882, https://doi.org/10.1016/j.energy.2021.122882.

[28] S. Yang, C. Zhang, J. Jiang, W. Zhang, Y. Gao, L. Zhang, A voltage reconstruction model based on partial charging curve for state-of-health estimation of lithium-ion batteries, J. Energy Storage 35 (2021) 102271, https://doi.org/10.1016/j.est.2021.102271.

[29] J. Schmitt, M. Rehm, A. Karger, A. Jossen, Capacity and degradation mode estimation for lithium-ion batteries based on partial charging curves at different current rates, J. Energy Storage 59 (2023) 106517, https://doi.org/10.1016/j.est.2022.106517.

[30] M. Dubarry, M. Berecibar, A. Devie, D. Anseán, N. Omar, I. Villarreal, State of health battery estimator enabling degradation diagnosis: model and algorithm description, J. Power Sources 360 (2017) 59–69, https://doi.org/10.1016/j.jpowsour.2017.05.121.

[31] M. Berecibar, M. Garmendia, I. Gandiaga, J. Crego, I. Villarreal, State of health estimation algorithm of $LiFePO_4$ battery packs based on differential voltage curves for battery management system application, Energy 103 (2016) 784–796, https://doi.org/10.1016/j.energy.2016.02.163.

[32] Y. Li, M. Abdel-Monem, R. Gopalakrishnan, M. Berecibar, E. Nanini-Maury, N. Omar, P. van den Bossche, J. Van Mierlo, A quick on-line state of health estimation method for Li-ion battery with incremental capacity curves processed by Gaussian filter, J. Power Sources 373 (2018) 40–53, https://doi.org/10.1016/j.jpowsour.2017.10.092.

[33] M. Lee, S. Kim, S. Kim, J.-I. Choi, Bilevel-optimized continual learning for predicting capacity degradation of lithium-ion batteries, J. Energy Storage 86 (2024) 111187, https://doi.org/10.1016/j.est.2024.111187.

[34] K.P. Lijesh, M.M. Khonsari, A thermodynamic approach for characterizing the degradation of Li-ion batteries, J. Energy Storage 82 (2024) 110565, https://doi.org/10.1016/j.est.2024.110565.

[35] H.M. Dahn, A.J. Smith, J.C. Burns, D.A. Stevens, J.R. Dahn, User-friendly differential voltage analysis freeware for the analysis of degradation mechanisms in Li-ion batteries, J. Electrochem. Soc. 159 (2012) A1405, https://doi.org/10.1149/2.013209jes.

[36] K. Honkura, K. Takahashi, T. Horiba, Capacity-fading prediction of lithium-ion batteries based on discharge curves analysis, J. Power Sources 196 (2011) 10141–10147, https://doi.org/10.1016/j.jpowsour.2011.08.020.

[37] M. Dubarry, B.Y. Liaw, M.-S. Chen, S.-S. Chyan, K.-C. Han, W.-T. Sie, S.-H. Wu, Identifying battery aging mechanisms in large format Li ion cells, J. Power Sources 196 (2011) 3420–3425, https://doi.org/10.1016/j.jpowsour.2010.07.029.

[38] B. Jiang, H. Dai, X. Wei, Incremental capacity analysis based adaptive capacity estimation for lithium-ion battery considering charging condition, Appl. Energy 269 (2020) 115074, https://doi.org/10.1016/j.apenergy.2020.115074.

[39] B. Pan, D. Dong, J. Wang, J. Nie, S. Liu, Y. Cao, Y. Jiang, Aging mechanism diagnosis of lithium ion battery by open circuit voltage analysis, Electrochim. Acta 362 (2020) 137101, https://doi.org/10.1016/j.electacta.2020.137101.

[40] A.D.A. Bin Abu Sofian, I.S. Imaduddin, S.R. Majid, T.A. Kurniawan, K.W. Chew, C.-H. Lay, P.L. Show, Nickel-rich nickel–cobalt–manganese and nickel–cobalt–aluminum cathodes in lithium-ion batteries: pathways for performance optimization, J. Clean. Prod. 435 (2024) 140324, https://doi.org/10.1016/j.jclepro.2023.140324.

[41] L. Ni, H. Chen, J. Gao, Y. Mei, H. Wang, W. Deng, G. Zou, H. Hou, X. Ji, Multiscale crystal field effect for high-performance ultrahigh-Ni layered cathode, ACS Nano 17 (2023) 12759–12773, https://doi.org/10.1021/acsnano.3c03770.

[42] Y. Zhou, H. Zhang, Y. Wang, T. Wan, P. Guan, X. Zhou, X. Wang, Y. Chen, H. Shi, A. Dou, M. Su, R. Guo, Y. Liu, L. Dai, D. Chu, Relieving stress concentration through anion–cation codoping toward highly stable nickel-rich cathode, ACS Nano 17 (2023) 20621–20633, https://doi.org/10.1021/acsnano.3c07655.

[43] M.A. Kebede, Ni-rich $LiNi_xCo_yM_{1\text{-}x\text{-}y}O_2$ (NCM; M=Mn, Al) cathode materials for lithium-ion batteries: challenges, mitigation strategies, and perspectives, Curr. Opin. Electrochem. 39 (2023) 101261, https://doi.org/10.1016/j.coelec.2023.101261.

[44] A.D.A. Bin Abu Sofian, I.S. Imaduddin, S.R. Majid, T.A. Kurniawan, K.W. Chew, C.-H. Lay, P.L. Show, Nickel-rich nickel–cobalt–manganese and nickel–cobalt–aluminum cathodes in lithium-ion batteries: pathways for performance optimization, J. Clean. Prod. 435 (2024) 140324, https://doi.org/10.1016/j.jclepro.2023.140324.

[45] L. Hou, Q. Liu, X. Chen, Q. Yang, D. Mu, L. Li, F. Wu, R. Chen, In-depth understanding of the deterioration mechanism and modification engineering of high energy density Ni-rich layered lithium transition-metal oxide cathode for lithium-ion batteries, Chem. Eng. J. 465 (2023) 142946, https://doi.org/10.1016/j.cej.2023.142946.

[46] B.S. Lee, S.-H. Oh, Y.J. Choi, M.-J. Yi, S.H. Kim, S.-Y. Kim, Y.-E. Sung, S.Y. Shin, Y. Lee, S.-H. Yu, SiO-induced thermal instability and interplay between graphite and SiO in graphite/SiO composite anode, Nat. Commun. 14 (2023) 150, https://doi.org/10.1038/s41467-022-35769-2.

[47] J.B. Goodenough, K.-S. Park, The Li-ion rechargeable battery: a perspective, J. Am. Chem. Soc. 135 (2013) 1167–1176, https://doi.org/10.1021/ja3091438.

[48] J.R. Dahn, E.W. Fuller, M. Obrovac, U. von Sacken, Thermal stability of $LixCoO_2$, Li_xNiO_2 and λ-MnO_2 and consequences for the safety of Li-ion cells, Solid State Ionics 69 (1994) 265–270, https://doi.org/10.1016/0167-2738(94)90415-4.

[49] S.S. Zhang, Problems and their origins of Ni-rich layered oxide cathode materials, Energy Storage Mater. 24 (2020) 247–254, https://doi.org/10.1016/j.ensm.2019.08.013.

[50] D. Li, D.L. Danilov, B. Zwikirsch, M. Fichtner, Y. Yang, R.-A. Eichel, P.H.L. Notten, Modeling the degradation mechanisms of $C_6/LiFePO_4$ batteries, J. Power Sources 375 (2018) 106–117, https://doi.org/10.1016/j.jpowsour.2017.11.049.

[51] D. Li, H. Li, D. Danilov, L. Gao, J. Zhou, R.-A. Eichel, Y. Yang, P.H.L. Notten, Temperature-dependent cycling performance and ageing mechanisms of $C_6/LiNi_{1/3}Mn_{1/3}Co_{1/3}O_2$ batteries, J. Power Sources 396 (2018) 444–452, https://doi.org/10.1016/j.jpowsour.2018.06.035.

[52] J.S. Edge, S. O'Kane, R. Prosser, N.D. Kirkaldy, A.N. Patel, A. Hales, A. Ghosh, W. Ai, J. Chen, J. Yang, S. Li, M.-C. Pang, L.B. Diaz, A. Tomaszewska, M. Waseem Marzook, K.N. Radhakrishnan, H. Wang, Y. Patel, B. Wu, G.J. Offer, Lithium ion battery degradation: what you need to know, Phys. Chem. Chem. Phys. 23 (2021) 8200–8221, https://doi.org/10.1039/D1CP00359C.

[53] N. Takenaka, A. Bouibes, Y. Yamada, M. Nagaoka, A. Yamada, Frontiers in theoretical analysis of solid electrolyte interphase formation mechanism, Adv. Mater. 33 (2021) 2100574, https://doi.org/10.1002/adma.202100574.

[54] J. Wu, M. Ihsan-Ul-Haq, Y. Chen, J.-K. Kim, Understanding solid electrolyte interphases: advanced characterization techniques and theoretical simulations, Nano Energy 89 (2021) 106489, https://doi.org/10.1016/j.nanoen.2021.106489.

[55] G. Kucinskis, M. Bozorgchenani, M. Feinauer, M. Kasper, M. Wohlfahrt-Mehrens, T. Waldmann, Arrhenius plots for Li-ion battery ageing as a function of temperature, C-rate, and ageing state – an experimental study, J. Power Sources 549 (2022) 232129, https://doi.org/10.1016/j.jpowsour.2022.232129.

[56] Y. Gao, S. Yang, J. Jiang, C. Zhang, W. Zhang, X. Zhou, The mechanism and characterization of accelerated capacity deterioration for Lithium-ion battery with $Li(NiMnCo)O_2$ cathode, J. Electrochem. Soc. 166 (2019) A1623, https://doi.org/10.1149/2.1001908jes.

[57] E. Sarasketa-Zabala, I. Gandiaga, L.M. Rodriguez-Martinez, I. Villarreal, Calendar ageing analysis of a $LiFePO_4$/graphite cell with dynamic model validations: towards realistic lifetime predictions, J. Power Sources 272 (2014) 45–57, https://doi.org/10.1016/j.jpowsour.2014.08.051.

[58] P. Keil, A. Jossen, Calendar aging of NCA lithium-ion batteries investigated by differential voltage analysis and coulomb tracking, J. Electrochem. Soc. 164 (2016) A6066, https://doi.org/10.1149/2.0091701jes.

[59] I. Zilberman, J. Sturm, A. Jossen, Reversible self-discharge and calendar aging of 18650 nickel-rich, silicon-graphite lithium-ion cells, J. Power Sources 425 (2019) 217–226, https://doi.org/10.1016/j.jpowsour.2019.03.109.

[60] M. Dubarry, M. Berecibar, A. Devie, D. Anseán, N. Omar, I. Villarreal, State of health battery estimator enabling degradation diagnosis: model and algorithm description, J. Power Sources 360 (2017) 59–69, https://doi.org/10.1016/j.jpowsour.2017.05.121.

[61] D. Anseán, G. Baure, M. González, I. Cameán, A.B. García, M. Dubarry, Mechanistic investigation of silicon-graphite/$LiNi_{0.8}Mn_{0.1}Co_{0.1}O_2$ commercial cells for non-intrusive diagnosis and prognosis, J. Power Sources 459 (2020) 227882, https://doi.org/10.1016/j.jpowsour.2020.227882.

[62] K.P.C. Yao, J.S. Okasinski, K. Kalaga, J.D. Almer, D.P. Abraham, Operando quantification of (de)lithiation behavior of silicon–graphite blended electrodes for lithium-ion batteries, Adv. Energy Mater. 9 (2019) 1803380, https://doi.org/10.1002/aenm.201803380.

[63] M.-T.F. Rodrigues, Z. Yang, S.E. Trask, A.R. Dunlop, M. Kim, F. Dogan, B. Key, I. Bloom, D.P. Abraham, A.N. Jansen, Pouch cells with 15% silicon calendar-aged for 4 years, J. Power Sources 565 (2023) 232894, https://doi.org/10.1016/j.jpowsour.2023.232894.

[64] J. Wang, J. Purewal, P. Liu, J. Hicks-Garner, S. Soukazian, E. Sherman, A. Sorenson, L. Vu, H. Tataria, M.W. Verbrugge, Degradation of lithium ion batteries employing graphite negatives and nickel–cobalt–manganese oxide + spinel manganese oxide positives: part 1, aging mechanisms and life estimation, J. Power Sources 269 (2014) 937–948, https://doi.org/10.1016/j.jpowsour.2014.07.030.

[65] Z. Chen, D.L. Danilov, Q. Zhang, M. Jiang, J. Zhou, R.-A. Eichel, P.H.L. Notten, Modeling NCA/C_6-Si battery ageing, Electrochim. Acta 430 (2022) 141077, https://doi.org/10.1016/j.electacta.2022.141077.

[66] C.R. Birkl, M.R. Roberts, E. McTurk, P.G. Bruce, D.A. Howey, Degradation diagnostics for lithium ion cells, J. Power Sources 341 (2017) 373–386, https://doi.org/10.1016/j.jpowsour.2016.12.011.

[67] A. Bordes, D.L. Danilov, P. Desprez, A. Lecocq, G. Marlair, B. Truchot, M. Dahmani, C. Siret, S. Laurent, S. Herreyre, A. Dominget, L. Hamelin, G. Rigobert, S. Benjamin, N. Legrand, M. Belerrajoul, W. Maurer, Z. Chen, L.H.J. Raijmakers, D. Li, J. Zhou, P.H.L. Notten, P. Perlo, M. Biasiotto, R. Introzzi, M. Petit, J. Martin, J. Bernard, S. Koffel, V. Lorentz, E. Durling, S. Kolari, Z. Wang, M. Massazza, S. Lamontarana, A holistic contribution to fast innovation in electric vehicles: an overview of the DEMOBASE research project, eTransportation 11 (2022) 100144, https://doi.org/10.1016/j.etran.2021.100144.

[68] D. Li, D.L. Danilov, L. Gao, Y. Yang, P.H.L. Notten, Degradation mechanisms of $C_6/LiFePO_4$ batteries: experimental analyses of cycling-induced aging, Electrochim. Acta 210 (2016) 445–455, https://doi.org/10.1016/j.electacta.2016.05.091.

[69] A.J. Smith, J.C. Burns, X. Zhao, D. Xiong, J.R. Dahn, Publisher's note: a high precision coulometry study of the SEI growth in Li/graphite cells [J. Electrochem. Soc., 158, A447 (2011)], J. Electrochem. Soc. 158 (2011) S23, https://doi.org/10.1149/1.3608243.

[70] B. Wu, C. Chen, L.H.J. Raijmakers, J. Liu, D.L. Danilov, R.-A. Eichel, P.H.L. Notten, Li-growth and SEI engineering for anode-free Li-metal rechargeable batteries: a review of current advances, Energy Storage Mater. 57 (2023) 508–539, https://doi.org/10.1016/j.ensm.2023.02.036.

[71] D. Li, D. Danilov, Z. Zhang, H. Chen, Y. Yang, P.H.L. Notten, Modeling the SEI-formation on graphite electrodes in $LiFePO_4$ batteries, J. Electrochem. Soc. 162 (2015) A858–A869, https://doi.org/10.1149/2.0161506jes.

[72] X. Zhao, Y. Yin, Y. Hu, S.-Y. Choe, Electrochemical-thermal modeling of lithium plating/stripping of $Li(Ni_{0.6}Mn_{0.2}Co_{0.2})O_2$/Carbon lithium-ion batteries at subzero ambient temperatures, J. Power Sources 418 (2019) 61–73, https://doi.org/10.1016/j.jpowsour.2019.02.001.

[73] D. Anseán, M. Dubarry, A. Devie, B.Y. Liaw, V.M. García, J.C. Viera, M. González, Operando lithium plating quantification and early detection of a commercial $LiFePO_4$ cell cycled under dynamic driving schedule, J. Power Sources 356 (2017) 36–46, https://doi.org/10.1016/j.jpowsour.2017.04.072.

[74] A.J. Crawford, D. Choi, P.J. Balducci, V.R. Subramanian, V.V. Viswanathan, Lithium-ion battery physics and statistics-based state of health model, J. Power Sources 501 (2021) 230032, https://doi.org/10.1016/j.jpowsour.2021.230032.

[75] A.A. Tahmasbi, M.H. Eikerling, Statistical physics-based model of mechanical degradation in lithium ion batteries, Electrochim. Acta 283 (2018) 75–87, https://doi.org/10.1016/j.electacta.2018.06.119.

[76] Y. Zhao, P. Stein, Y. Bai, M. Al-Siraj, Y. Yang, B.-X. Xu, A review on modeling of electro-chemo-mechanics in lithium-ion batteries, J. Power Sources 413 (2019) 259–283, https://doi.org/10.1016/j.jpowsour.2018.12.011.

[77] M. Haruta, T. Okubo, Y. Masuo, S. Yoshida, A. Tomita, T. Takenaka, T. Doi, M. Inaba, Temperature effects on SEI formation and cyclability of Si nanoflake powder anode in the presence of SEI-forming additives, Electrochim. Acta 224 (2017) 186–193, https://doi.org/10.1016/j.electacta.2016.12.071.

[78] D. Li, H. Li, D.L. Danilov, L. Gao, X. Chen, Z. Zhang, J. Zhou, R.-A. Eichel, Y. Yang, P.H.L. Notten, Degradation mechanisms of $C_6/LiNi_{0.5}Mn_{0.3}Co_{0.2}O_2$ Li-ion batteries unraveled by non-destructive and post-mortem methods, J. Power Sources 416 (2019) 163–174, https://doi.org/10.1016/j.jpowsour.2019.01.083.